Article

Bioinspired capillary force-driven super-adhesive filter

Junyong Park[1,6], Chan Sik Moon[1,6], Ji Min Lee[1], Sazzadul A. Rahat[2], Sang Moon Kim[3], Jonathan T. Pham[2,4], Michael Kappl[5], Hans-Jürgen Butt[5] & Sanghyuk Wooh[1✉]

Capturing particles with low, nanonewton-scale adhesion is an ongoing challenge for conventional air filters[1,2]. Inspired by the natural filtration abilities of mucus-coated nasal hairs[3,4], we introduce an efficient, biomimetic filter that exploits a thin liquid coating. Here we show that a stable thin liquid layer is formed on several filter media that generates enhanced particulate adhesion, driven by micronewton to sub-micronewton capillary forces[5,6]. Enhanced particle adhesion increases the filtration of airborne particulates while maintaining air permeability, providing longer filter lifetime and increased energy savings. Moreover, strong adhesion of the captured particles enables effective filtration under high-speed airflow as well as suppression of particle redispersion. We anticipate that these filters with thin liquid layers afford a new way to innovate particulate matter filtering systems.

Air filters, designed to capture airborne particulate matter (PM), are present in every aspect of our lives, from air purifiers for residential housing to industrial filters for cleanrooms[7,8]. The adhesion between PM and conventional filters is primarily governed by van der Waals interactions and is typically of the order of nanonewtons. This low adhesion can be insufficient to capture and retain PMs, causing poor filtration. Issues arising from weak adhesion have remained unsolved for decades and continue to be a limitation in filtration performance.

A nasal cavity, which includes nasal hairs, effectively filters PM by strong adhesion (Fig. 1a). The key element facilitating PM adhesion is a thin mucus layer that coats the nasal hairs. When PM encounters the mucus, a meniscus forms, generating strong adhesion by capillarity. The filtration ability of mucus-coated nasal hair is demonstrated by exposing it to pollen-laden air (Supplementary Fig. 1); an optical microscope image of the hair confirmed that pollen adheres onto the surface by mucus (Fig. 1b). Inspired by this filtration mechanism, we introduce a bioinspired filter having a thin liquid layer. This liquid is an oil, which increases adhesion for enhanced particulate removal from air. We term this the particle-removing oil-coated filter (PRO filter). For decades, there have been efforts to apply liquids onto filters to enhance filtering performance[9–13]. Previous research shows that enhanced filtration efficiencies (FEs) have been exhibited by liquid soaking; at the same time, pressure drops were also increased because of blocked pores by the liquid (Supplementary Table 1). Moreover, unstably coated oil was easily detached from the filter surface by air flow. As a result, liquid-incorporating filters have been used for only limited applications, such as engine air filtering. For widespread use, it is necessary to create a thin, uniform, stable coating of a non-volatile liquid on the surface of a filter. A long-term stable, thin liquid layer was previously demonstrated with tri-methylsiloxy-terminated polydimethylsiloxane (PDMS; for example, silicone oil) on a PDMS brush-grafted surface[14,15]. This method has been used to fabricate lubricant-infused surfaces having thin lubricant layers. Because of the mobile lubricant, liquid drops or solid particles easily slide off the surface with low friction in the lateral direction[16–18], finding applications in areas such as anti-icing[19], anti-biofouling[20,21] and liquid-drop manipulation[22]. However, in the vertical direction (that is, normal to the surface), lubricant can induce strong adhesion, mainly facilitated by capillary forces[6,23]. This unique characteristic is exploited in the present study for effective capture of PM.

General approach and comparative performance

PDMS brushes with a thickness of about 10 nm are covalently grafted on the surface of different filter media by polymerization of dimethyldimethoxysilane from surface hydroxyl groups[24] (Extended Data Fig. 1). Silicone oil is then applied onto the PDMS brush-grafted filter by spraying a silicone oil solution in hexane. Hexane is used to precisely control the thickness of the oil layer. In principle, this spraying process can also be performed with only oil or oil in water emulsion to exclude any toxicity issue. After the hexane evaporates, a thin, uniform silicone oil layer is formed (Fig. 1c). Because the PDMS brush and silicone oil are chemically identical, the interfacial energy is minimized. The spreading coefficient (S) is positive, making silicone oil spontaneously spread across the filter media (that is, $\gamma_S > \gamma_{SL} + \gamma_L$, where γ is the interfacial energy at solid–air, solid–liquid and liquid–air interfaces). The scanning electron microscope (SEM) image in Fig. 1d confirms a homogeneous, thin oil layer on polyester fibres without issues from Plateau–Rayleigh instabilities[25]. This thin liquid layer does not notably influence the pore structure. The air permeability of the oil-coated filter (325.6 ± 4.0 cm^3 s^{-1} cm^{-2}) is nearly identical to the uncoated filter (322.7 ± 6.0 cm^3 s^{-1} cm^{-2}).

Despite similarities in air permeability, the PRO filter demonstrates superior performance in capturing PM. As a comparative analysis,

[1]Department of Chemical Engineering, Chung-Ang University, Seoul, Republic of Korea. [2]Department of Mechanical and Materials Engineering, University of Cincinnati, Cincinnati, OH, USA. [3]Department of Mechanical Engineering, Incheon National University, Incheon, Republic of Korea. [4]Department of Chemical and Environmental Engineering, University of Cincinnati, Cincinnati, OH, USA. [5]Max Planck Institute for Polymer Research, Mainz, Germany. [6]These authors contributed equally: Junyong Park, Chan Sik Moon. ✉e-mail: woohsh@cau.ac.kr
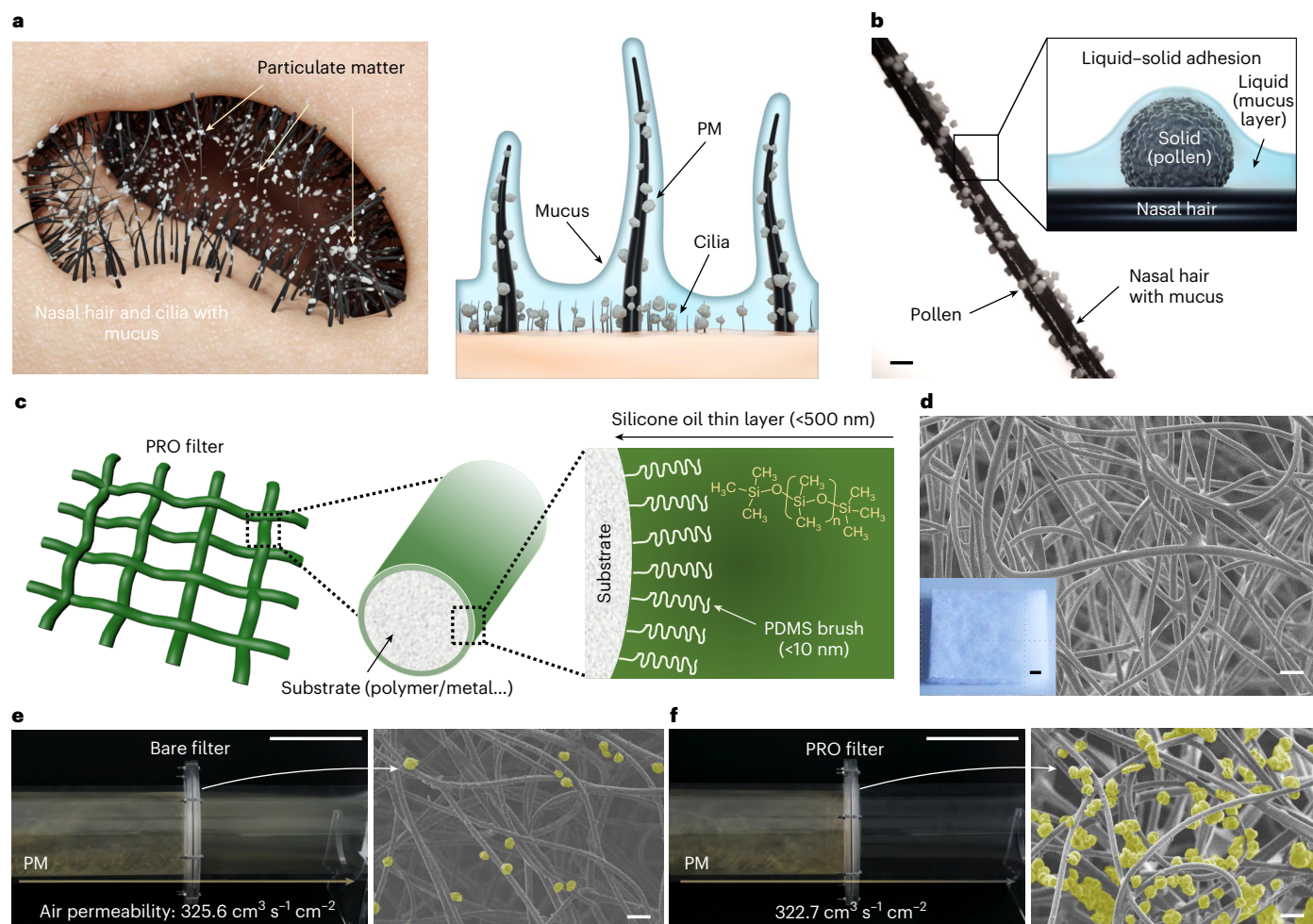
Fig. 1 | Super-adhesive biomimetic adhesion-enhanced liquid film filter.
a, Schematic of the mechanism of dust particle adhesion in the nasal cavity, mediated by mucus-coated hairs. **b**, Photograph of the nasal hair capturing dust on the mucus layer. **c**,**d**, Schematic overview (**c**) and SEM image (**d**) of the PRO filter, modelled on the adhesive characteristics of nasal hairs. Inset of **d** is a photograph of the filter. **e**,**f**, Filtration in cylindrical wind tunnel with bare filters (**e**) and PRO polyester filters (**f**). Air permeability was measured at 125 Pa following the standard of ASTM D737. Pictures on the right are SEM images of the filter after filtration, showing trapped dust particles. Scale bars, 100 μm (**b**,**d**,**e**, right; **f**, right); 1 cm (**d**, inset); 10 cm (**e**, left; **f**, left).

around 50 μm pollens were blown into conventional, non-woven filters with a pore size of 100–500 μm (Supplementary Video 1). Most of the pollen particles are not filtered and pass through the filter (Fig. 1e). An SEM image of the filter after filtration confirms that pollens were rarely captured by the filter fibres. By contrast, most pollen is filtered by the PRO filter (Fig. 1f). The silicone oil layer acts similarly to mucus on nasal hair, resulting in strong adhesion between the pollen and fibres. This contrast exhibits the positive effect of the thin liquid layer on enhancing PM capture.

Filtration efficiency

The FE is quantitatively investigated with a custom-built air filter testing chamber (Supplementary Fig. 4). The chamber is designed to quantify two parameters: (1) PM concentrations and (2) the pressure drop across the filter. The FEs for filters of varying materials and media types with different pore sizes are shown in Fig. 2a. These efficiencies are categorized into three distinct size groups relevant to inhalable PM causing adverse health effects: $PM_{1.0}$ (0.3–1.0 μm), $PM_{2.5}$ (1.0–2.5 μm), and PM_{10} (2.5–10 μm). Orange bars represent FEs of bare filters, and green bars represent FEs of PRO filters. The application of a thin oil layer leads to FE enhancements of 10–30% compared with the bare counterparts. This improvement is

achieved with almost no change in air permeability (Extended Data Table 1).

The liquid layers are submicrometre in thickness, resulting in negligible changes in the diameters of fibres (about 5–100 μm). For example, in the case of a polyester filter with a fibre diameter of 39.2 ± 1.0 μm, 10 g m^{-2} of silicone oil is estimated to form a coating of approximately 500 nm in thickness, increasing the total diameter by 2.5%. Consequently, the pressure drop is nearly unchanged from before to after the application of the liquid layer (smaller than 3% difference). It should be noted that increasing the liquid layer thickness could clog the pores. However, our findings indicate that such a thick layer is not required for the PRO filter because FE enhancements are already maximized at liquid layer thicknesses of just a few hundred nanometres (Extended Data Fig. 2). The optimum liquid quantity required to achieve maximum FE enhancement, while minimally affecting pressure drop, varies according to the specific filter medium.

Particle adhesion

To better understand the effect of a thin oil layer on filter efficiency, we measured single-particle adhesion on thin oil layers using the colloidal probe atomic force microscopy (AFM). This is useful for measuring adhesion in the normal direction by approaching and retracting a
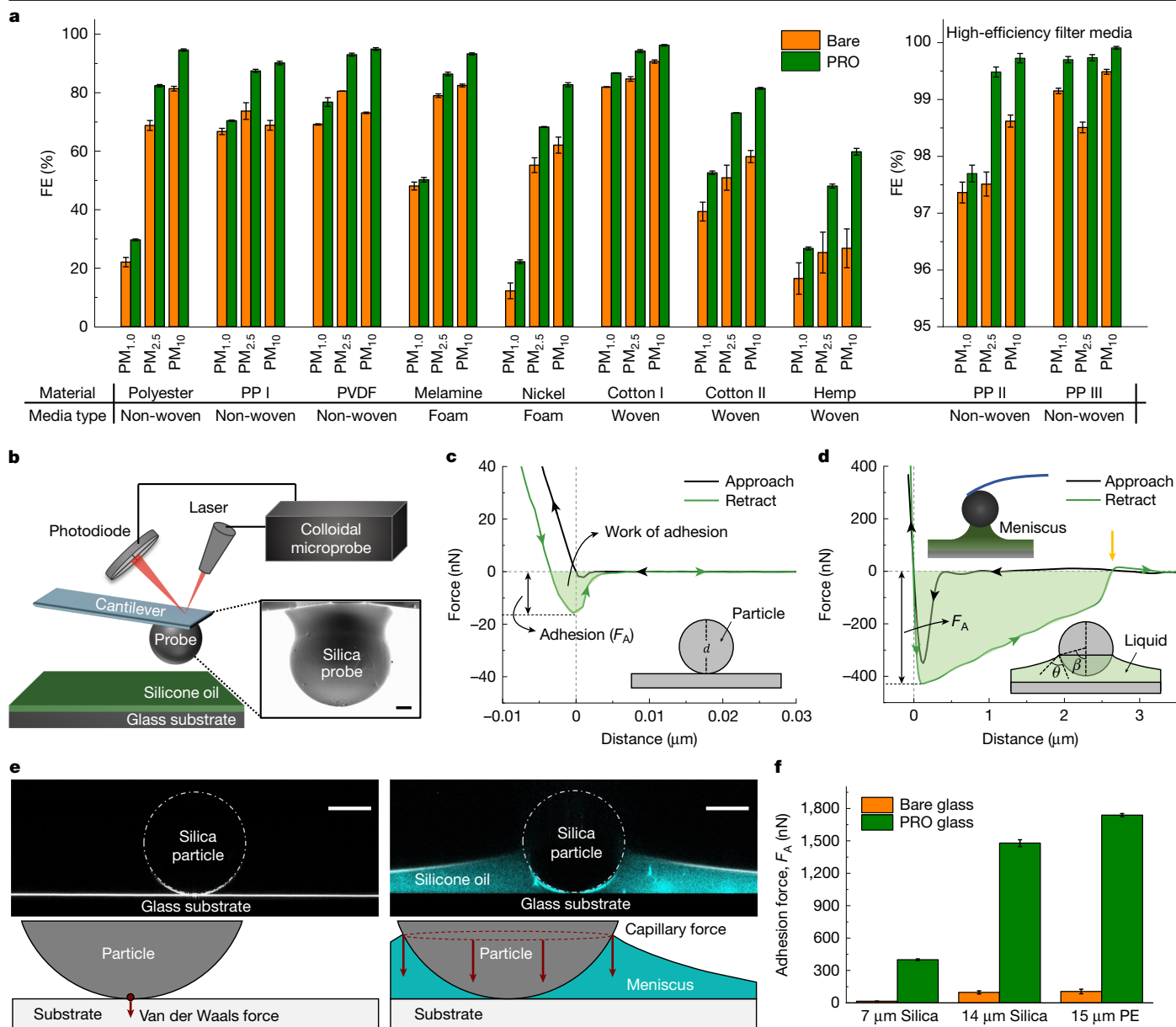
Fig. 2 | Filtration performance and microparticle adhesion. a, FEs of different filters. Detailed numerical metrics such as air permeability, FE and pressure drop are provided in Extended Data Table 1. Error bars show s.d.; $n = 3$. PP, polypropylene. **b**, Schematic of the colloidal microprobe technique. Inset indicates a silica probe (about 7 µm) glued on a tipless cantilever, characterized by SEM. **c**,**d**, Force–distance curves measured on bare (**c**) and PRO (**d**) glass substrates. Bidirectional arrow and highlighted area represent the adhesion force (F_A) and the work of adhesion of particles, respectively. **e**, Confocal microscopy images of microparticles on bare (left) and PRO (right) glass. **f**, Adhesion forces of microparticles interacting with bare and PRO glass. Error bars show s.d.; $n = 3$. PE, polyethylene. Scale bars, 1 µm (**b**, inset); 50 µm (**e**).

particle from planar substrates[26] (Fig. 2b). Given that the diameter of typical airborne PMs ranges from 0.3 µm to 20 µm, we selected microparticles with diameters between 7 µm and 15 µm as probes. Force–distance curves include the adhesion force (F_A), which is the most negative force recorded during retraction (Extended Data Fig. 3b). To detach a particle, this adhesion force must be overcome. As a control, we first measured particle adhesion on flat bare glass; the adhesion force of a 7.1 ± 0.9 µm silica particle was 15 ± 0.9 nN (Fig. 2c). Hard particles predominantly interact with solid substrates by van der Waals force with a range of 2–50 nN for an approximately 7 µm particle (Supplementary Information section 5). For a model system of the PRO filter, we use a glass substrate uniformly coated with silicone oil (viscosity 100 cSt (centistokes)) having a thickness of 203 ± 2 nm, referred to here as PRO glass. On PRO glass, the adhesion force increased

to 400 ± 8 nN, which is around 25 times greater than that on bare glass (Fig. 2d).

This enhanced adhesion is attributed to the formation of a liquid meniscus[27]. Confocal microscopy images show that an oil meniscus forms between the silica particle and the PRO glass (Fig. 2e). When a solid particle contacts a liquid layer, the liquid wets the particle, promptly creating a meniscus that generates a capillary force. The capillary force induced by the meniscus on a sphere is governed by the equation $F_C = \pi \gamma d \sin(\beta) \sin(\beta + \theta)$, where γ is the surface tension, d is the particle diameter, θ is the contact angle and β is the filling angle that describes the location of the three-phase contact line on the particle (Fig. 2d). Capillary force between a particle and a thin liquid layer is generally one to two orders of magnitude greater than van der Waals force. These findings agree with our measured adhesion forces[28].
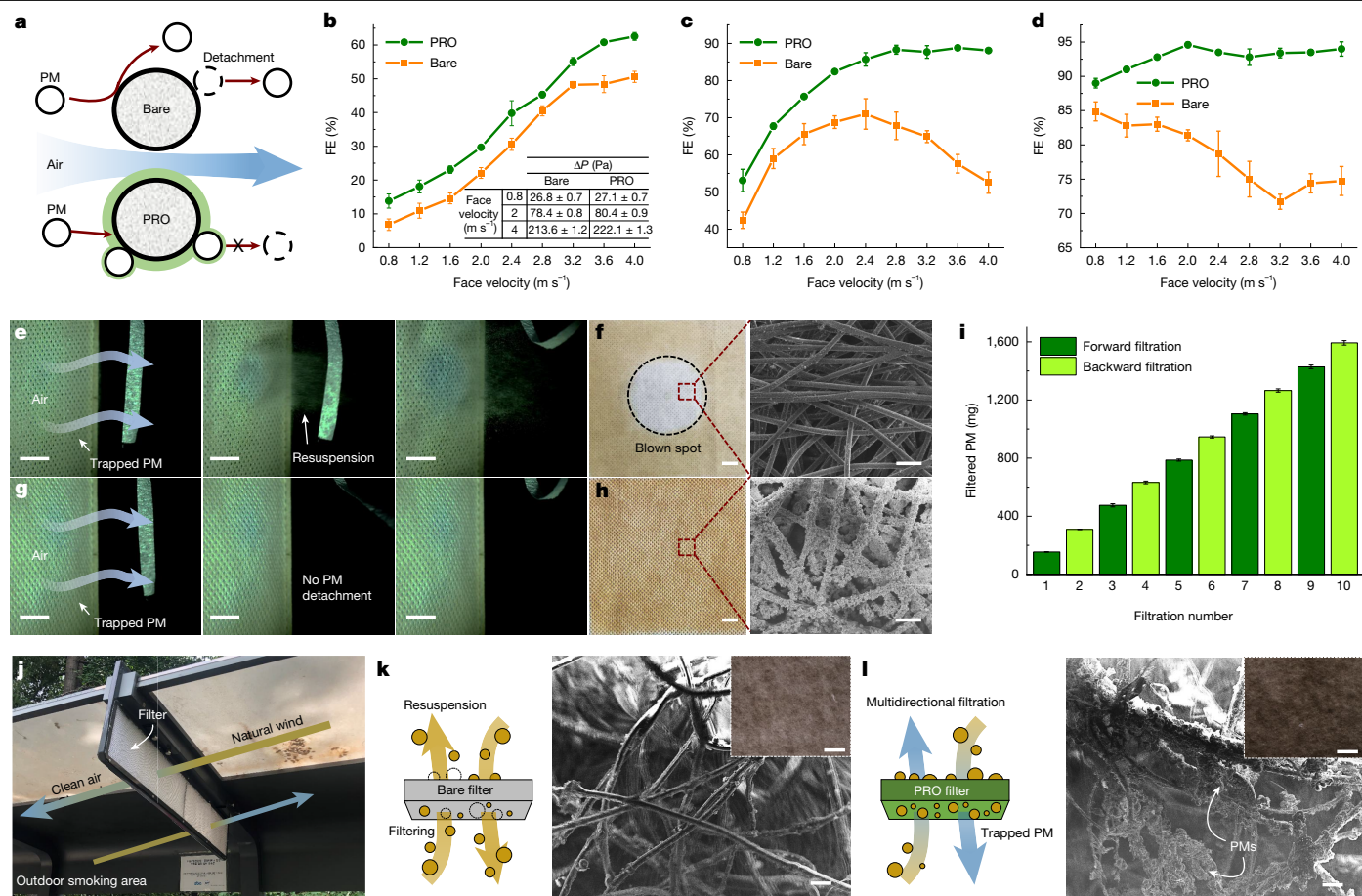
Fig. 3 | Capillary force-driven PM filtration with suppressed bouncing: rapid airflow filtration and suppressed PM resuspension. a, Schematic of PM capturing behaviours on bare (top) and PRO (bottom) fibres. **b**–**d**, FEs of polyester filters for $PM_{1.0}$ (**b**), $PM_{2.5}$ (**c**) and PM_{10} (**d**) across diverse face velocities. Error bars show s.d.; $n = 3$. Inset in **b** includes pressure drops corresponding to face velocities before filtration. **e**,**g**, High-speed camera images of PM-filtered bare (**e**) and PRO (**g**) filters when airflow in the reverse direction is applied: 0 ms (left); 40 ms (middle); and 80 ms (right). **f**,**h**, Photographic (left) and SEM (right) images presenting bare (**f**) and PRO (**h**) filters after air sweeping. **i**, Bidirectional PM filtration of the PRO filter. At each cycle, the filter was inverted after measuring the weights of captured PMs. Then, about 170 mg PM was applied again through 2 m s^{-1} airflow. Error bars show s.d.; $n = 3$. **j**, Photograph of multidirectional filtering set-up at a smoking area. **k**,**l**, SEM images of bare (**k**) and PRO (**l**) filters after 38 months of installation (14 July 2021 to 28 September 2024) at the smoking area. Inset pictures are the photos of filters. Scale bars, 1 cm (**e**,**g**); 1 cm (**f**, left; **h**, left); 200 μm (**f**, right; **h**, right); 100 μm (**k**,**l**); 2 cm (**k**, inset; **l**, inset).

The work of adhesion was also characterized from the area above the retraction curve (Fig. 2c,d, bright green area). The work of adhesion on bare glass was 0.2 ± 0.03 fJ, whereas it reached 730 ± 34 fJ on PRO glass. During retraction on bare glass, the force precipitously drops to zero after a short distance, as van der Waals interactions are confined to a few nanometres. Conversely, the PRO glass holds onto the particle until the liquid meniscus ruptures about 2.5 μm from the substrate (Fig. 2d, yellow arrow). Hence, this capillary adhesion mechanism is effective over micrometre-range distances, resulting in an adhesion energy that is three to four orders of magnitude higher than bare glass.

Furthermore, the enhancement in adhesion due to the thin liquid layer is observed for both 14.0 ± 3.4 μm silica and 15.4 ± 2.4 μm polyethylene spheres (Fig. 2f and Supplementary Fig. 8). Larger particles have higher adhesion force on both bare glass and PRO glass because both van der Waals and capillary forces are proportional to the particle size. The hydrophobicity of the particles has a modest influence on adhesion force, as evidenced by a comparison between hydrophilic silica and hydrophobic polyethylene particles. Enhanced adhesion is observed for both silica and polyethylene spheres (Fig. 2f and Supplementary Fig. 8). The shape and size of the meniscus can be varied by the interfacial energy with particles, leading to differences in adhesion forces[29,30]. Nevertheless, it is noteworthy that all tested particles interacting with the thin liquid layer exhibit micronewton-scale adhesion forces, which are sufficiently high for effective capture of PM.

In terms of liquid layer thickness, we found that only a few hundred nanometres is sufficient for capillary force-assisted adhesion (Extended Data Fig. 4d). A layer of about 200 nm realizes sufficiently high adhesion force and work of adhesion, although thicker layers require more work to detach particles (Extended Data Fig. 4e). This thickness effect on adhesion matches our FE results shown in Extended Data Fig. 2. For this reason, 200–500 nm thick layers are mainly applied to filter media to realize maximum FE while minimizing the pressure drop.

Filtration at rapid airflow

Owing to its outstanding adhesion for PMs, the PRO filter offers unique filtration abilities, including efficient filtration under high-speed airflow. As the face velocity of airflow increases, the probability of PMs interacting with filter fibres rises, potentially elevating the FE[31,32]. However, the FE of a conventional filter generally diminishes beyond a certain airflow speed because of PMs detaching from filter fibres[33,34] (Fig. 3a). This occurs when the drag force surpasses the adhesion force. As the drag force increases with airflow speed, PMs detach more easily under faster airflows. Conventional filters are less efficient at fast

airflows, demonstrated by FE measurements using a conventional polyester filter (Fig. 3b–d). Numerical calculations corroborate that drag forces surpass the adhesion forces for all PMs, ranging from 0.3 μm to 10 μm, on conventional filters at airflows faster than 3 m s^{-1} (Extended Data Fig. 5); this highlights the limitations of conventional air filters in rapid filtration systems. By contrast, the FEs of PRO polyester filters increase for all PM sizes with increasing airflow velocity. Owing to the elevated PM adhesion, the PRO filter overcomes the issue of particle detachment.

PM resuspension

In conventional filtration systems, captured PMs often detach by external airflow, resulting in PM resuspension into the air. For example, PMs trapped on a conventional filter are detached when air is blown through the filter by an air gun, as observed by a high-speed camera (Fig. 3e and Supplementary Video 2). After blowing air, the detachment of PMs is observed by photography and SEM (Fig. 3f). By contrast, the PRO filter retains PMs when subjected to the same airflow (Fig. 3g and Supplementary Video 2), without a change in the PRO filter colour (Fig. 3h).

Owing to issues of resuspension, conventional filtration systems typically operate only under unidirectional airflow. To illustrate the multidirectional airflow functionality of PRO filters, we measured the weight of filtered PMs after filtration tests in opposite directions (Fig. 3i). Following an initial filtration, the PRO filter is inverted and exposed to an equivalent quantity of PMs introduced from the reverse side. Nearly the same weight increase was observed owing to PM capture without resuspension. This filtration process continues to function for more than five cycles. Multidirectional filtration was further demonstrated by installing the PRO filters in an outdoor smoking area without the use of any external fan (Fig. 3j). An SEM image of the bare filter showed only a few captured PMs after being installed for 38 months, because most captured PMs got resuspended by wind (Fig. 3k). The colour change of the bare filter to brown was mostly caused by staining from tobacco aerosol residue. By contrast, many PMs were strongly captured by the PRO filters without resuspension, confirmed by bundles of PMs inside the PRO filter and by the dark brown colour (Fig. 3l). This is the first instance of a multidirectional filtration strategy proposing a zero-energy filtration system that uses natural wind.

Pressure drop increase by PM filtration

The thin liquid film in the PRO filter provides advantages in the (1) lifetime of the filter and (2) energy consumption of the filtration system. Both are related to pore clogging. Accumulation of PM within the pore leads to an increase in the pressure drop (ΔP) across the filter. This pressure increase is particularly profound in filters with smaller pore sizes, such as high-efficiency particulate air (HEPA) filters. A PRO HEPA filter exhibits approximately 25% slower rate of ΔP increase compared with a bare HEPA filter, shown as grey and black lines in Fig. 4a, respectively. The underlying reason for this reduced rate of ΔP increase can be attributed to the distinctive structure in which PMs are captured (Supplementary Video 3). On conventional filters, PMs form dendrites during filtration. The PM dendrites have a large effective thickness (t_{eff}) because of its loosely packed structure (Fig. 4b), leading to pore clogging[35]. An image of a planar metal mesh shows a decrease in pore size because of captured PMs (Fig. 4c and Extended Data Fig. 6); analysis shows a reduction in the projected pore area fraction (that is, projection pore area per unit area) from 0.35 mm^2 mm^{-2} to 0.21 mm^2 mm^{-2}. By contrast, PMs captured on the PRO filter are densely packed by capillary forces (Fig. 4d). This dense arrangement minimizes the effective thickness of the filter medium. Observations on a PRO metal mesh confirm a slower rate of increase in the effective thickness (Fig. 4e and Extended Data Fig. 6). The projected pore area fraction is reduced only to 0.30 mm^2 mm^{-2}, keeping pores approximately 43% more open

compared with the bare metal mesh, effectively mitigating the rate of ΔP increase.

To reduce the rate of ΔP increase, filtration systems commonly use a multiple-filter strategy, involving a combination of low- and high-efficiency filters. The low-efficiency pre-filter has relatively large pores capable of capturing large PMs. The pre-capturing of large PMs prevents clogging of small pores on high-efficiency filters, such as HEPA filters. The incorporation of a bare pre-filter in front of an HEPA filter exhibits a reduced rate of ΔP increase by approximately 1.8 times compared with a stand-alone HEPA filter (Fig. 4a, orange and black lines). We proposed that effective filtration by a PRO pre-filter would suppress clogging of an HEPA filter (Fig. 4f). A PRO pre-filter offers an even slower rate of ΔP increase (Fig. 4a, blue line).

To understand the filter system design, we conducted a comparative analysis of the mass of captured PMs using different filter combinations. Although the total mass of captured PMs by both the PRO pre-filter and bare HEPA filter and the bare pre-filter and bare HEPA filter was nearly identical because of the almost 99.9% FE of the HEPA filter, the distribution of captured PMs differed substantially. When used with the PRO pre-filter, the HEPA filter contained 63% less captured PMs compared with the bare pre-filter. This is because the PRO pre-filter captures 48% more PMs than the bare pre-filter (Fig. 4g, blue and orange bars). The images on the right side of Fig. 4g show the bare and PRO pre-filters following the filtration process. The darker colour of the PRO pre-filter indicates enhanced PM capturing. By integrating effective pre-capturing and capillary-driven densification of PMs, the combination of a PRO pre-filter and PRO HEPA filter (Fig. 4a, green line) shows the longest time of use. For example, the PRO combination delays the time needed to double ΔP by three times compared with the bare combination (Fig. 4a, orange line), suggesting that PRO filters offer three times longer lifetimes.

Reusability and real-world testing

Following the filtration process, PRO filters can be regenerated after washing. The thin silicone oil layer can be washed with detergent water, thereby removing captured PMs (Extended Data Fig. 7). The grafted PDMS brush remains on the surface after washing. Therefore, by a simple oil spraying process, a thin, uniform silicone oil layer reforms, restoring the initial filtration performance of the PRO filter. The reusability of the PRO filters offers a notable reduction in filter waste.

This superior performance of PRO filters was demonstrated in field filtration tests performed by installation in HVAC (heating, ventilation and air conditioning) systems at various sites (Fig. 4h and Extended Data Fig. 8). Before the field filtration tests, stability of PRO filters under humid condition was verified by exposing the filters to boiling water. Even after exposing it to the extremely humid condition with airborne water droplets for 3 h, the PRO filter still performed similarly to the fresh-made PRO filter, promising applicability in the real environment (Supplementary Fig. 12). Practical operation in an indoor baseball stadium for 180 days showed that the PRO filter captured 42% more PMs by weight than a conventional filter. Although the PRO filters capture more PMs, the PRO filters exhibited 58% slower pressure drop enhancement by effective pre-capturing and capillary-driven densification. As a result, the electric consumption of the fans in the ventilation system is reduced by up to 27%, and the filter life is prolonged more than twice (Fig. 4i,j). These field tests in real filtration conditions confirm that the PRO filters with stable, thin liquid layers offer substantial practical advantages over conventional filter systems.

Discussion

Although previous studies have attempted to enhance filtering performance with liquid coatings, the inherent instability of these films can lead to pore clogging and liquid detachment. Our PRO filters offer a transformative advance in filtration technology, facilitated by the
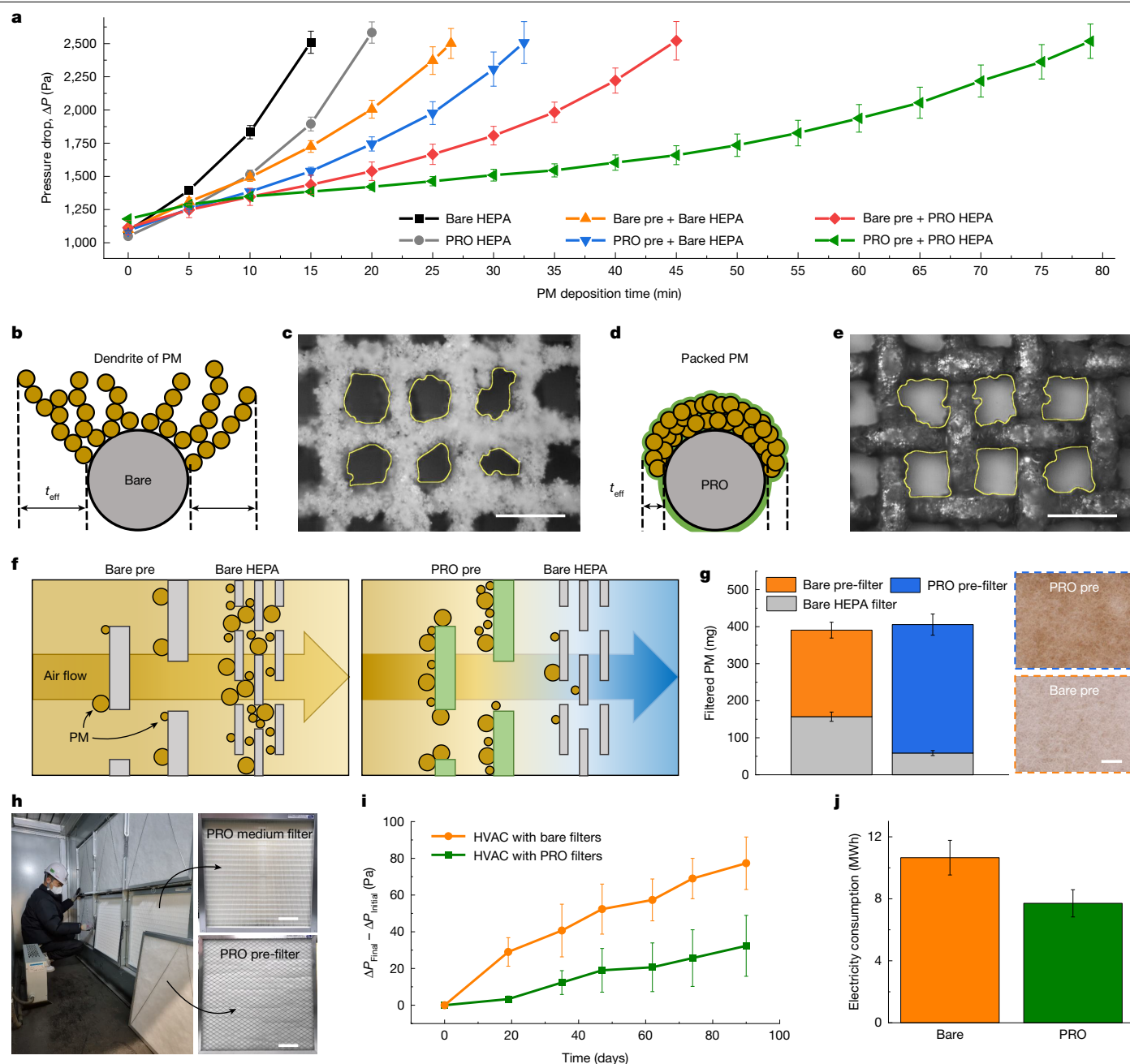
Fig. 4 | Pressure drop by filter. a, Pressure drop curves during PM filtration. Error bars show s.d.; $n = 3$. **b**–**e**, Structures of captured PMs. Schematic of captured PMs on solid (**b**) and thin liquid-layered (**d**) filter media. The term t_{eff} represents the average distance from the fibre to the extremity of the PM accumulation. Optical microscope images of captured PMs, each with approximately 200 mg on bare (**c**) and PRO (**e**) metal meshes. The contour of pores is shown with a yellow line. **f**, Schematics of the PM screening by bare (left) and PRO (right) pre-filters for an HEPA filter. **g**, Weights of captured PMs on pre-filters and HEPA filters after the filtration test using the combinations of pre-filters and HEPA filters. Orange, blue and grey boxes indicate PMs on bare

pre-filter, PRO pre-filter and HEPA filter. Error bars show s.d.; $n = 3$. The images on the right show the bare and PRO pre-filters after filtration with the HEPA filter. **h**, Photos of filters installed in the HVAC system; top right and bottom right are medium and pre-filters, respectively. **i**, Pressure drop difference across the HVAC system with bare (orange line) and PRO (green line) filters (26 May 2023 to 24 August 2023). Error bars show s.d.; $n = 3$. **j**, Electricity consumed by the fan of the HVAC systems for the same period operated with the bare (orange bar) and the PRO (green bar) filters. Error bars show s.d.; $n = 3$. Scale bars, 100 μm (**c**,**e**); 1 cm (**g**, right); 10 cm (**h**, right).

formation of a stable, thin liquid layer on the filter media, enabled by PDMS brush grafting[9–13]. The PRO filters minimize PM bouncing, leading to outstanding FE at rapid airflows, making PRO filters a suitable candidate for applications requiring rapid and large-scale filtration. Captured PMs are strongly adhered to the filter media by the thin liquid layer, suppressing PM resuspension and preventing re-contamination of air; this also enables multidirectional air filtration capabilities, such as passive, zero-energy filtration by natural airflow. Moreover, the slower

rate of increase in ΔP extends the operational lifetime of PRO filters and minimizes energy consumption, even as it filters a greater volume of PMs. The remarkable performance of PRO filters in practical-scale ventilation systems confirms a marked reduction in energy consumption and better PM capture, demonstrating substantial advantages over conventional filters in real-world applications. It is anticipated that the strategy of thin oil-coated filters will provide opportunities for a new model of environment-friendly PM filters.

Article

Online content

Any methods, additional references, Nature Portfolio reporting summaries, source data, extended data, supplementary information, acknowledgements, peer review information; details of author contributions and competing interests; and statements of data and code availability are available at https://doi.org/10.1038/s41586-025-09156-y.

1. Maus, R. & Umhauer, H. Collection efficiencies of coarse and fine dust filter media for airborne biological particles. *J. Aerosol Sci.* **28**, 401–415 (1997).
2. Li, W. et al. Study of particle rebound and deposition on fibre surface. *Environ. Technol.* **41**, 691–702 (2018).
3. Fahy, J. V. & Dickey, B. F. Airway mucus function and dysfunction. *N. Engl. J. Med.* **363**, 2233–2247 (2010).
4. Cone, R. A. Barrier properties of mucus. *Adv. Drug Deliv. Rev.* **61**, 75–85 (2009).
5. Glover, J. D. & Pham, J. T. Capillary-driven indentation of a microparticle into a soft, oil-coated substrate. *Soft Matter* **16**, 5812–5818 (2020).
6. Schellenberger, F. et al. Detaching microparticles from a liquid surface. *Phys. Rev. Lett.* **121**, 048002 (2018).
7. Zhang, G.-H. et al. High-performance particulate matter including nanoscale particle removal by a self-powered air filter. *Nat. Commun.* **11**, 1653 (2020).
8. Kwon, H. J. et al. Long-lifetime water-washable ceramic catalyst filter for air purification. *Nat. Commun.* **14**, 520 (2023).
9. Müller, T. K., Meyer, J., Thébault, E. & Kasper, G. Impact of an oil coating on particle deposition and dust holding capacity of fibrous filters. *Powder Technol.* **253**, 247–255 (2014).
10. Maddineni, A. K., Das, D. & Damodaran, R. M. Inhibition of particle bounce and re-entrainment using oil-treated filter media for automotive engine intake air filtration. *Powder Technol.* **322**, 369–377 (2017).
11. Raie, M. S., Rakhshandehroo, G. & Mooselu, M. G. Experimental performance evaluation of a filter coated with castor oil for particulate matter absorption (PM$_{2.5}$ and PM$_{10}$). *Water Air Soil Pollut.* **234**, 633 (2023).
12. Yadav, S. & Das, D. Liquid-mediated particle capture by nonwoven filter media for automotive engine intake air filtration. *J. Ind. Text.* **51**, 5658S–5682S (2022).
13. Rao, A. K. & Whitby, K. T. Non-ideal collection characteristics of inertial impactors—I. Single-stage impactors and solid particles. *J. Aerosol Sci.* **9**, 77–86 (1978).
14. Wooh, S. & Butt, H. J. A photocatalytically active lubricant-impregnated surface. *Angew. Chem. Int. Ed.* **56**, 4965–4969 (2017).
15. Chen, L. et al. One-step fabrication of universal slippery lubricated surfaces. *Adv. Mater. Interfaces* **7**, 2000305 (2020).
16. Wong, T.-S. et al. Bioinspired self-repairing slippery surfaces with pressure-stable omniphobicity. *Nature* **477**, 443–447 (2011).
17. You, I., Lee, T. G., Nam, Y. S. & Lee, H. Fabrication of a micro-omnifluidic device by omniphilic/omniphobic patterning on nanostructured surfaces. *ACS Nano* **8**, 9016–9024 (2014).
18. Vogel, N., Belisle, R. A., Hatton, B., Wong, T.-S. & Aizenberg, J. Transparency and damage tolerance of patternable omniphobic lubricated surfaces based on inverse colloidal monolayers. *Nat. Commun.* **4**, 2176 (2013).
19. Wilson, P. W. et al. Inhibition of ice nucleation by slippery liquid-infused porous surfaces (SLIPS). *Phys. Chem. Chem. Phys.* **15**, 581–585 (2013).
20. Wang, P., Zhang, D., Lu, Z. & Sun, S. Fabrication of slippery lubricant-infused porous surface for inhibition of microbially influenced corrosion. *ACS Appl. Mater. Interfaces* **8**, 1120–1127 (2016).
21. Amini, S. et al. Preventing mussel adhesion using lubricant-infused materials. *Science* **357**, 668–673 (2017).
22. Hwang, H., Papadopoulos, P., Fujii, S. & Wooh, S. Driving droplets on liquid repellent surfaces via light-driven Marangoni propulsion. *Adv. Funct. Mater.* **32**, 2111311 (2022).
23. Li, J., Li, W., Tang, X., Han, X. & Wang, L. Lubricant-mediated strong droplet adhesion on lubricant-impregnated surfaces. *Langmuir* **37**, 8601–8615 (2021).
24. Wang, L. & McCarthy, T. J. Covalently attached liquids: instant omniphobic surfaces with unprecedented repellency. *Angew. Chem. Int. Ed.* **55**, 244–248 (2016).
25. Wang, P. et al. Bioinspired anti-Plateau-Rayleigh-instability on dual parallel fibers. *Adv. Mater.* **32**, e2003453 (2020).
26. Butt, H.-J., Cappella, B. & Kappl, M. Force measurements with the atomic force microscope: technique, interpretation and applications. *Surf. Sci. Rep.* **59**, 1–152 (2005).
27. Butt, H.-J. & Kappl, M. *Surface and Interfacial Forces* 2nd edn (Wiley, 2018).
28. Sun, W., Neuzil, P., Kustandi, T. S., Oh, S. & Samper, V. D. The nature of the gecko lizard adhesive force. *Biophys. J.* **89**, L14–L17 (2005).
29. Gennes, P.-G., Brochard-Wyart, F. & Quéré, D. *Capillarity and Wetting Phenomena: Drops, Bubbles, Pebbles, Waves* (Springer, 2004).
30. Rahat, S. A., Chaudhuri, K. & Pham, J. T. Capillary detachment of a microparticle from a liquid–liquid interface. *Soft Matter* **19**, 6247–6254 (2023).
31. Hinds, W. C. *Aerosol Technology: Properties, Behavior, and Measurement of Airborne Particles* (Wiley, 2012).
32. Thomas, D., Charvet, A., Bardin-Monnier, N. & Appert-Collin, J. C. *Aerosol Filtration* (Elsevier, 2016).
33. Dunn, P. F. & Renken, K. J. Impaction of solid aerosol particles on fine wires. *Aerosol Sci. Technol.* **7**, 97–107 (1987).
34. Konstandopoulos, A. G. Particle sticking/rebound criteria at oblique impact. *J. Aerosol Sci.* **37**, 292–305 (2006).
35. Chen, S., Liu, W. & Li, S. Effect of long-range electrostatic repulsion on pore clogging during microfiltration. *Phys. Rev. E* **94**, 063108 (2016).

Methods

Fabrication of thin liquid layer on filter media

Non-volatile, low surface tension tri-methylsiloxy-terminated PDMS (for example, silicone oil) was used for the thin liquid coating. Because the silicone oil can uniformly form a thin layer on a PDMS brush-grafted surface because of minimized interfacial energy, we prepared the PDMS brush onto the surface of filter media. Before the PDMS grafting, surface oxidation was initially performed using a UV–ozone cleaner (AhTech LTS), emitting ultraviolet light at a wavelength of 254 nm with an intensity of 20 mW cm^{-2}, for 15 min. Then, a solution including dimethyldimethoxysilane (96%, Gelest) and sulfuric acid (98%, Daejung Chemicals) dissolved in methanol (99.5%, Samchun Chemicals), weight ratio of 10:1:100, was sprayed onto the oxidized substrate. After evaporation of the solvent, the PDMS brush was synthesized from the surface hydroxyl groups by grafting from reaction. After the surface polymerization, residual unreacted chemicals were washed away using methanol. The presence of the grafted PDMS brush on various filter surfaces was confirmed by X-ray photoelectron spectroscopy (XPS) (K-alpha+, Thermo Fisher Scientific).

On the PDMS brush-grafted filter media, silicone oil (Gelest) solution in hexane (99.5%, Sigma Aldrich) was sprayed by using a spray gun equipped with a 0.35-mm nozzle at a pressure of 0.5 mPa. To remove residual hexane, the samples were dried at room temperature for 24 h. Then, hexane negligibly remained because of its high volatility. Silicone oil was spread over the surface of the fibres, realizing the PRO filter. To verify the incorporation of silicone oil within the filter media, an energy-dispersive X-ray spectroscopy analysis was conducted using a field-emission scanning electron microscope (FE-SEM) (SIGMA, Carl Zeiss).

Adhesion force analysis

The interaction between the spherical particle and a planar substrate was quantified using colloidal probe AFM (NanoWizard, JPK Instruments). Silica (about 7 μm and 15 μm) and polyethylene beads (around 15 μm, Cospheric) were used as probe particles, which were glued onto the edges of tipless cantilevers (MikroMasch) using epoxy glue. Before adhering the particle to the cantilever, the spring constant and sensitivity value of the cantilever were calibrated using a non-contact method. The force–distance curves were measured three times for each sample with a working speed of the cantilever of 2 μm s^{-1}.

For consistent analysis, adhesion was measured on planar samples. Cover glass (VWR Chemicals) was adopted as a substrate. Oil-coated substrate was prepared using a spin coater (ACE-200, iNexus) at a speed of 4,000 rpm for a duration of 60 s. The thickness of the silicone oil layer was varied by using different concentrations of silicone oil solution in n-hexane (95%, VWR Chemicals).

The force–distance curve, ascertained by observing cantilever deflection, allowed for the quantification of these forces. Extended Data Fig. 3 shows the basic methodology for analysing force–distance curves, specifically in measuring the behaviour at solid–liquid interfaces. The analysis consisted of a sequence of steps: (1) approaching the lubricated surface; (2) contact with the lubricant; (3) penetrating the lubricant; (4) touching the glass substrate, thereby showing lubricant thickness; (5) pushing the cantilever until it reached the artificial force limit; (6) retracting from the substrate with a meniscus; and (7) detachment of the probe. We initiated direct contact between the probe and the solid substrate because of the thinness of silicone oil, making interfacial contact with the lubricant unfeasible. We pressed the probe to its force threshold after contact with the solid surface to standardize the contact depth with the solid substrate.

Imaging of interface between substrate and particle

A confocal microscope (Leica SP8, Leica) was used to visualize the particles attached to planar substrates. A spherical silica particle (Duke Scientific) with a diameter of about 105 μm was used for these observations. Perylenediimide dye was applied within the silicone oil to observe the silicone oil meniscus surrounding the particle.

Characterization of filtering performance

FE was measured using a custom-built air filter testing chamber that complies with the specifications delineated in the global testing standard: DIN 71460-1:2006. To validate the reliability of the custom-built air filter testing chamber, cross-validation of efficiency measurement with a certified testing agency (KITECH) was performed (Supplementary Fig. 5). Identical testing standards and test conditions were applied in both set-ups to ensure consistency and comparability. FE was determined according to the equation $FE = \frac{C_b - C_a}{C_b} \times 100$, where C_b and C_a denote the PM concentrations before and after filtration, respectively. A2 fine standard test dust, briefly called A2 dust (Powder Technology), with a predominant size distribution diameter of 0.3–10 μm, was selected as test PM. A particle generator (SAG 410, TOPAS) consistently injected the A2 dust into the chamber. For each test, 90 mg of A2 dust was introduced. Quantitative measurement of airborne particles was taken using a particle counter (11-A, GRIMM) that can measure particle sizes ranging from 0.25 μm to 32 μm in diameter. FEs were categorized into three sizes based on PM diameters: $PM_{1.0}$ (0.3–1 μm), $PM_{2.5}$ (1–2.5 μm) and PM_{10} (2.5–10 μm).

Moreover, the pressure drop (ΔP) across the filtration system was monitored using a pressure gauge (PTA202D, SCS). The threshold for the pressure gauge in our system was approximately 2,500 Pa because of fan operation limit. The system was programmed to automatically modulate the face velocity by adjusting the airflow rate in response to observed elevations in ΔP, monitored using a flow meter (CP213, KIMO). The working area of FE test was selected as 100 cm^2. The electrostatic charge present on the filter media was neutralized before the measurements. To evaluate the filtering performance, the quality factor (QF) was calculated by combining FE and ΔP as follows: $QF = -\frac{\ln(1 - FE)}{\Delta P}$ (Supplementary Fig. 7). The weight of captured PM on filters was measured to intuitively compare the filtering performance by comparing the weight before and after filtration (Supplementary Fig. 22).

Various conventional filters, including pre-filters, medium filters and HEPA filters made of non-woven polyester, polypropylene and polyvinylidene fluoride (PVDF) were used as test filter media. Media of various materials with different pore structures, such as melamine foam, nickel foam, and woven fabrics made of cotton and hemp, were also applied. Pore structure of each filter media was measured using SEM (Supplementary Fig. 6). Air permeability of the filter media was measured using an air permeability meter (ADE-580A, AND), in accordance with ASTM D737, involving a pressure of 125 Pa over an area of 38 cm^2.

Effect of oil viscosity

To provide optimal viscosity of silicone oil layer for filtration, the effect of oil viscosity on the particle adhesion and the FE was investigated. Initially, we tested the adhesion force with varied viscosities of silicone oil: 100 cSt, 1,000 cSt, 5,000 cSt and 10,000 cSt (Extended Data Fig. 4a). Film thickness was fixed as 200 nm and approximately 15 μm silica bead was selected as reference probe. The probe approached the oil-coated glass substrates and moved until it touched for 500 nN of load. Then, the probe retracted from the substrate. The working speed of the cantilever was fixed at 2 μm s^{-1}. Furthermore, we tested the effect of oil viscosity on filtering performance at 2 m s^{-1} of face velocity (Supplementary Fig. 16). A polyester and polypropylene filter were used, and approximately 10 g m^{-2} of silicone oil was applied to synchronize other conditions. A detailed discussion of the effect of oil viscosity on filtering performance is provided in Supplementary Information section 4.

PM resuspension

To visualize the PM resuspension, a high-speed camera (FASTCAM SA6, Photron) operating at 1,000 frames per second was used (Fig. 3e,g). Nitrogen gas was blown by an air gun from the opposite direction to

Article

the A2 dust-capturing polypropylene non-woven filter. A piece of paper was positioned in front of the filter media as an indicator to confirm the blown gas through the filter. PM adhesion properties of filters during resuspension test were observed through SEM (Supplementary Fig. 20). Quantitative analysis of PM detachment was tested by placing the particle counter in front of PM-filtered filters during resuspension (Supplementary Fig. 21). Furthermore, PM resuspension in wide perspective was measured using digital camera (EOS D80, Canon) under blue light (Supplementary Fig. 23). Nitrogen gas was also blown by air gun from the opposite direction to the A2 dust captured polyester non-woven filter.

Multidirectional filtration

Multidirectional filtration characteristics were tested under (1) bidirectional filtration, (2) random airflow and (3) natural winds. Initially, to quantitatively analyse multidirectional filtration, we measured the weight of filtered PMs after a filtration test at a face velocity of 2 m s^{-1}. Then, we performed another filtration test in the opposite direction by flipping the filter in the chamber and measured the weight of filtered PMs. Furthermore, we demonstrated filtration under random airflow (Supplementary Fig. 24). We prepared a sculpture made of the PRO filter in a closed chamber and filled the space with A2 dust using a particle generator. Random airflow was generated by fans on four sides in the chamber. After the filtration under random airflow, the filtered PM on the PRO sculpture was imaged using SEM. Moreover, multidirectional filtration was tested under natural winds. We integrated filter holders in the outdoor smoking area and installed PRO filters without an external fan. After the filtration for 38 months, we captured photos and SEM images of both bare and PRO filters.

Characterization of particle packing behaviour by silicone oil

Polyester fibre with a diameter of 75 μm was used to observe the particle packing behaviour on the thin silicone oil layer. A single stretched fibre was installed in the filter testing chamber, then PM was deposited on the fibre. After the deposition, silicone oil with a viscosity of 100 cSt was dropped at the edge of the fibre. Then, the particle packing behaviour was observed using an optical microscope (S39B, Microscopes). The effective thickness (t_{eff}) of PM was measured using ImageJ by taking the fibre diameter from the average thickness of the dust deposited polyester fibre.

Furthermore, the changes in pore size in the filter were measured using stainless steel metal mesh. Images before and after filtration of the metal mesh were captured using an optical microscope. The projected pore area was measured through ImageJ using the size analyser feature, then six pores were averaged.

Energy consumption of the ventilation system

Calculation of electricity consumption from the ΔP–deposition time curve was done using the equation in the ventilation standard: SPS-KACA-0026-7175:2017 (Supplementary Fig. 25). Energy consumption of ventilation is expressed as $W = \frac{Q_v \Delta \bar{P} t}{1,000\eta}$, where Q_v is the airflow of ventilation, η is fan efficiency and t is the operation time. An airflow rate of 0.9 m^3 s^{-1} and a fan efficiency of 0.5 were used following the ventilation standard. The operation time was selected as 27 min based on the moment at which the ΔP across the bare pre-filter and HEPA filter (orange line) doubled its initial value.

Data availability

The data supporting the findings of this study are available in the paper and the Supplementary Information. Source data are provided with this paper.

Author contributions J.P., C.S.M. and S.W. conceptualized the research. J.P. fabricated the materials. J.P., C.S.M. and J.M.L. tested the filtering performance. J.P. and S.A.R. characterized the adhesion force and J.T.P., M.K. and H.-J.B. supervised the analysis. J.P. and S.M.K. performed the numerical analysis. S.W. supervised the research. J.P., C.S.M. and S.W. wrote the original draft. All authors reviewed and edited the paper.
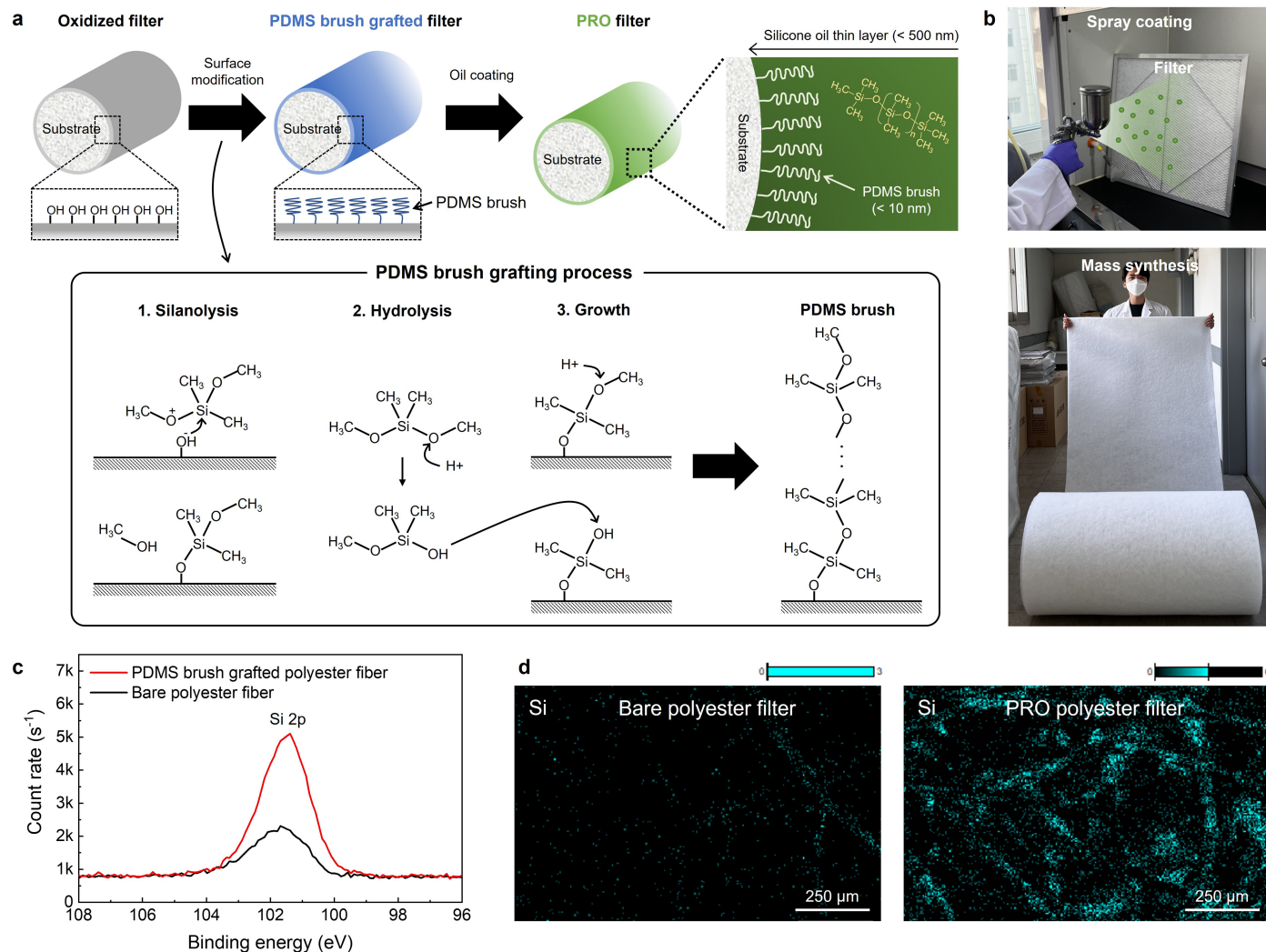
**Extended Data Fig. 1 | Fabrication method of the PRO filter and elemental characterization. a**, Schematics of fabrication procedure of the PRO filter. The box at the bottom explaining a schematic outline of the grafting process of PDMS brush. The PDMS brush grafting process consists of following sequential steps: silanolysis, hydrolysis, and growth of the PDMS brush. **b**, Photos depicting fabrication method using spray gun (top) and its mass production (bottom). **c**, XPS spectra indicating Si 2p element on the surface of bare (black line) and PDMS grafted (red line) polyester filter fiber. **d**, EDS analysis images representing Si of polyester filter. Left and right are bare and PRO filters, respectively.
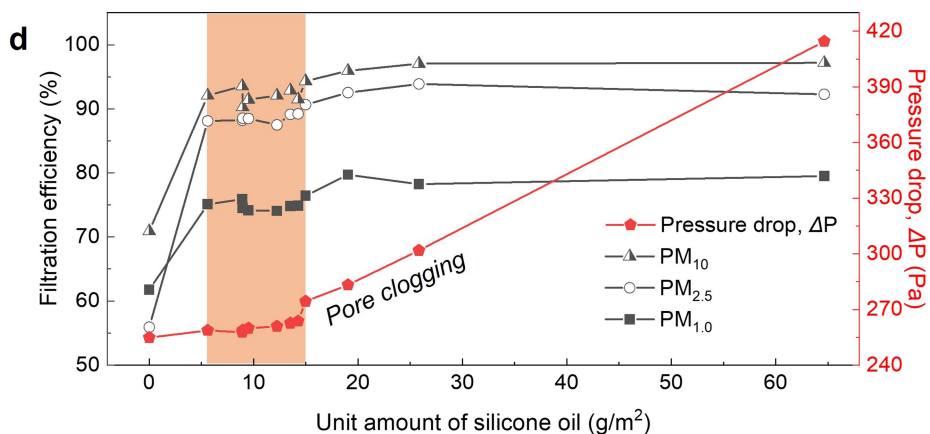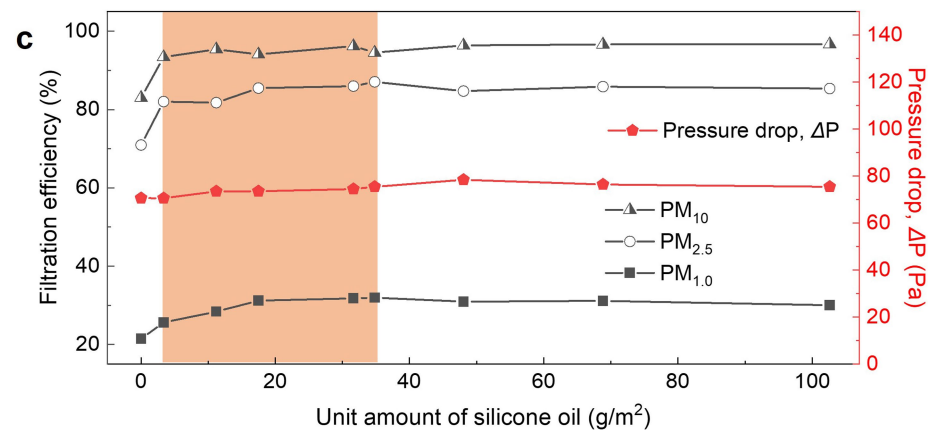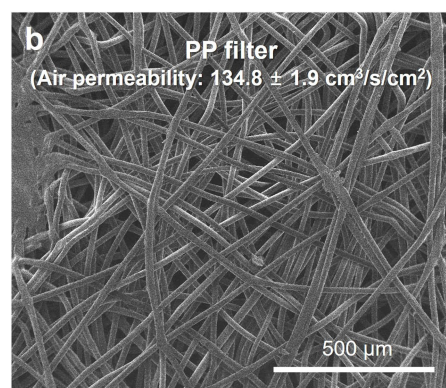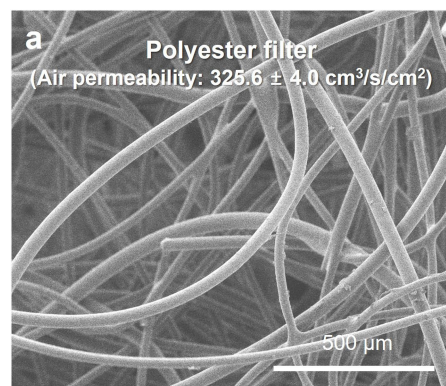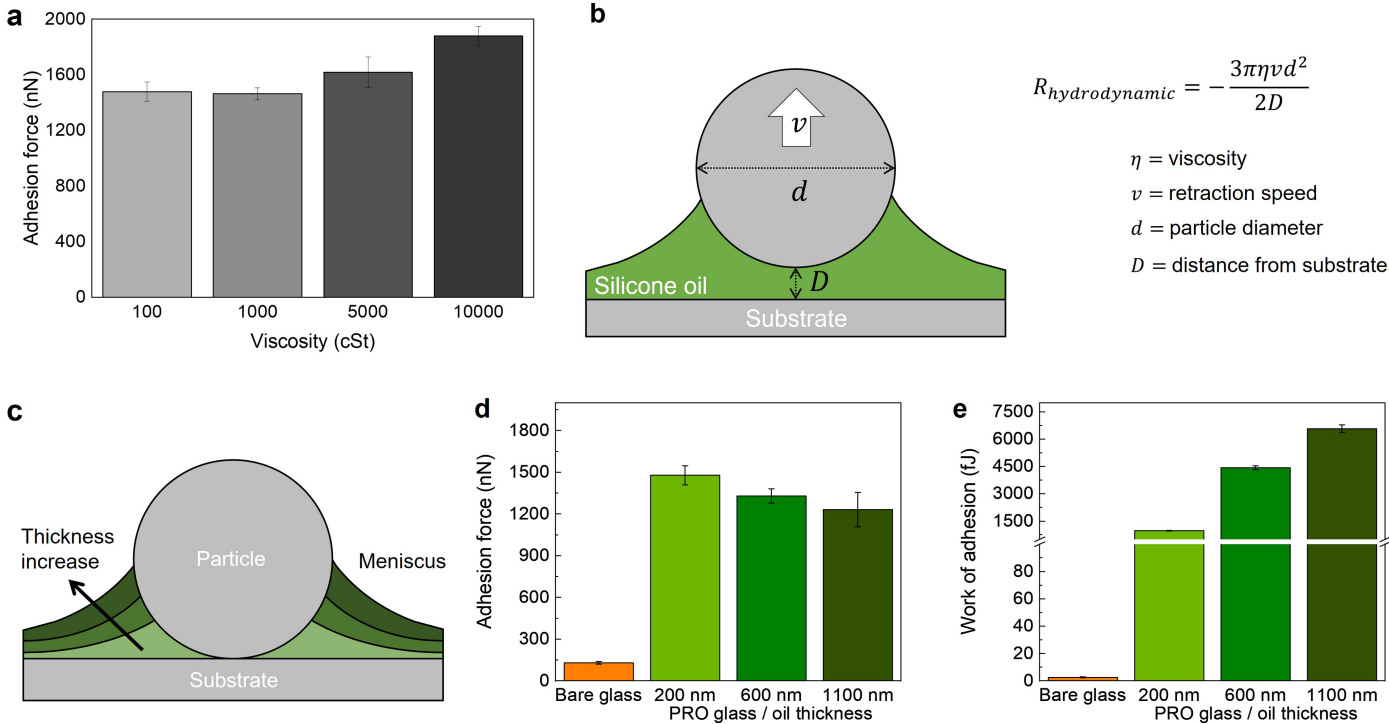
Extended Data Fig. 2 | Filtration performances with varied amounts of silicone oil. a,b, SEM images of polyester (**a**) and PP non-woven filters (**b**). **c,d**, Filtration performances of polyester (**c**) and PP filters (**d**) by coating amounts of silicone oil. Red and black lines representing ΔP and FEs of filter with 3 different size distributions, respectively. Orange boxes indicating optimum ranges of the amounts of silicone oil, achieving maximum FEs with negligible ΔP changes. Even though the ΔP of polyester filter was not elevated, we applied silicone oil of less than 35 g m^{-2} to avoid serious Plateau-Rayleigh instability at the fibers, as shown in Supplementary Fig. S3.
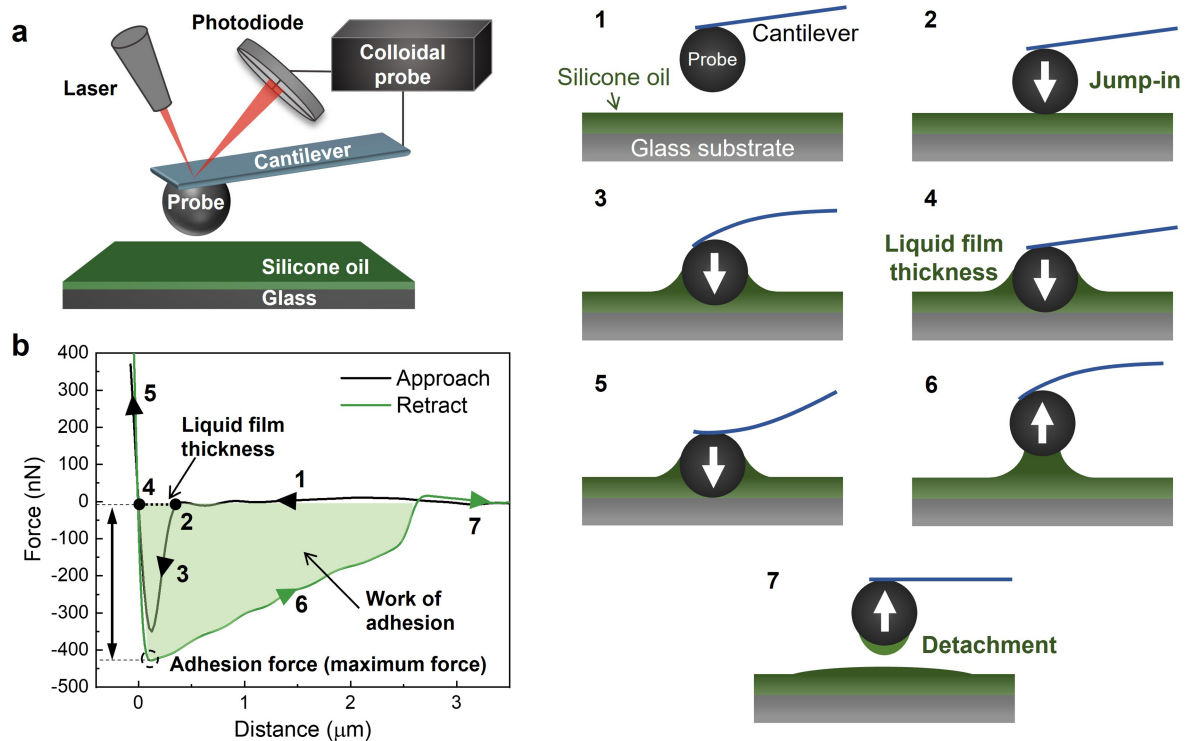
Extended Data Fig. 3 | Principles of colloidal probe-based force measurement. a,b, Schematic illustration of colloidal probe technique interacting with oil-coated substrate (**a**) and its force-distance curve (**b**). Numbers in the curve corresponding to each step are shown on the right images.

a

b

$$R_{hydrodynamic} = -\frac{3\pi\eta v d^2}{2D}$$

η = viscosity

v = retraction speed

d = particle diameter

D = distance from substrate

c

d

e

Extended Data Fig. 4 | Adhesion force of particle on varied thicknesses and viscosities of liquid layer. a, Adhesion forces with varied viscosities of silicone oil: 100, 1000, 5000, 10000 cSt. Errors show s.d.; n = 3. **b**, Schematic describing hydrodynamic resistance during particle retraction. Inset equation indicates hydrodynamic resistance induced by liquid film. **c**, Schematic to elucidate different size and shape of meniscus on various thickness of liquid film. **d**,**e**, Adhesion force (**d**) and work of adhesion (**e**) of bare (orange bar) and PRO (green bars) glass with varied liquid thickness, interacting with a 15 μm silica bead in diameter. Errors show s.d.; n = 3.
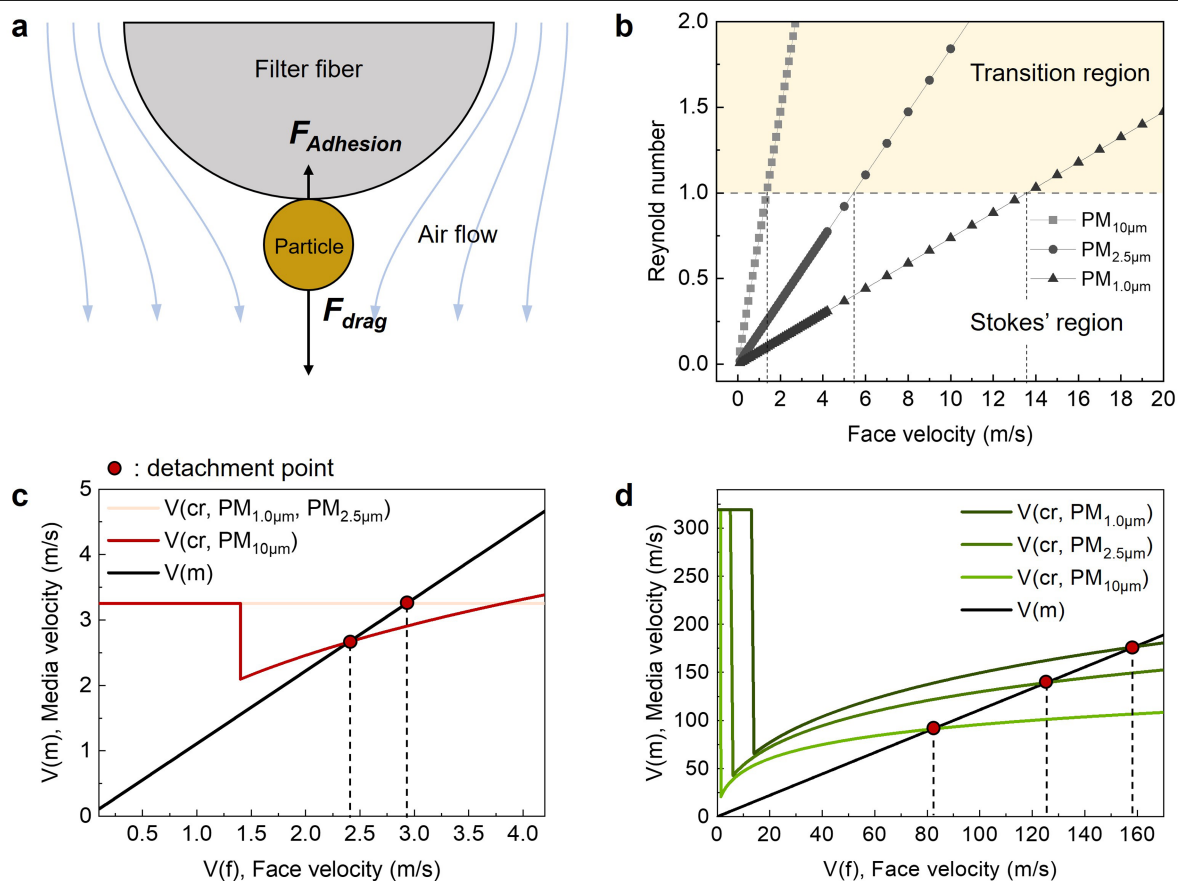
**Extended Data Fig. 5 | Particle resuspension critical velocity analysis.**
a, Schematic representing forces exerted on particles adhering to filter fiber.
Position of particle on filter fiber was postulated that it was repositioned along
the rounded surface of fiber by drag forces, as depicted. **b**, Reynolds numbers
corresponding to $PM_{1.0\mu m}$, $PM_{2.5\mu m}$, and $PM_{10\mu m}$ plotting as a function of face
velocity, with a demarcation at a Reynolds number of 1 to separate Stokes'

region from transition region. **c**,**d**, The theoretical computations for critical
detachment velocities $V_{(cr)}$ for bare (**c**) and PRO (**d**) filters as functions of
particle size and face velocity. Points of intersection between media velocity
$V_{(m)}$ and critical detachment velocity $V_{(cr)}$ are highlighted in red dots, indicating
the onset of particle detachment. Detailed numerical calculation corroborated
in Supplementary Information Section 5.
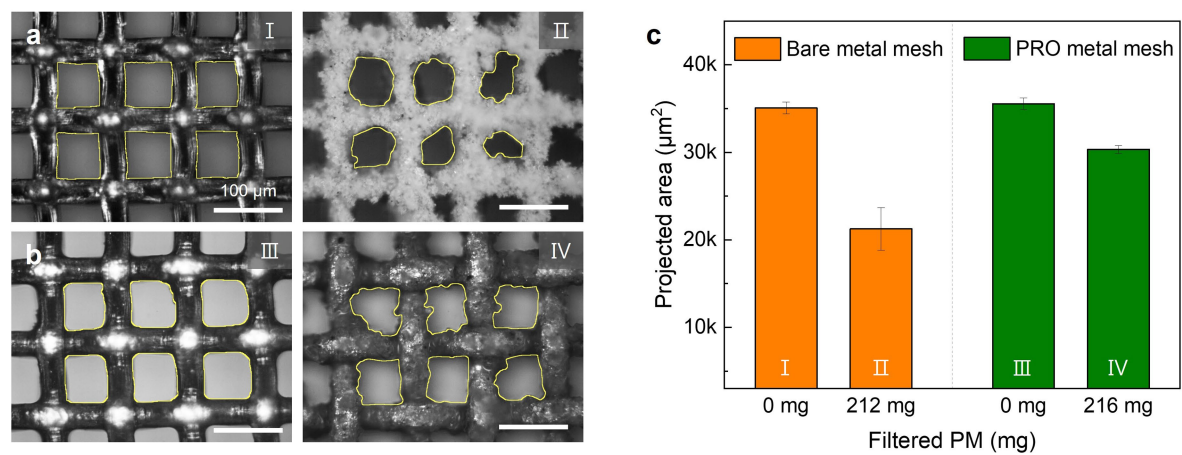
Extended Data Fig. 6 | Projection pore area analysis during filtration.
a,**b**, SEM images of the bare (**a**) and PRO (**b**) stainless steel metal mesh during filtration. Yellow boxes of each image represent the pores of metal meshes. **c**, Projected pore areas of metal mesh before (I and III) and after (II and IV) filtration. The weights of filtered PMs were similar, which was 212 mg on bare and 216 mg on PRO metal mesh over unit area of 100 cm^2. Error bars show s.d.; $n = 6$.
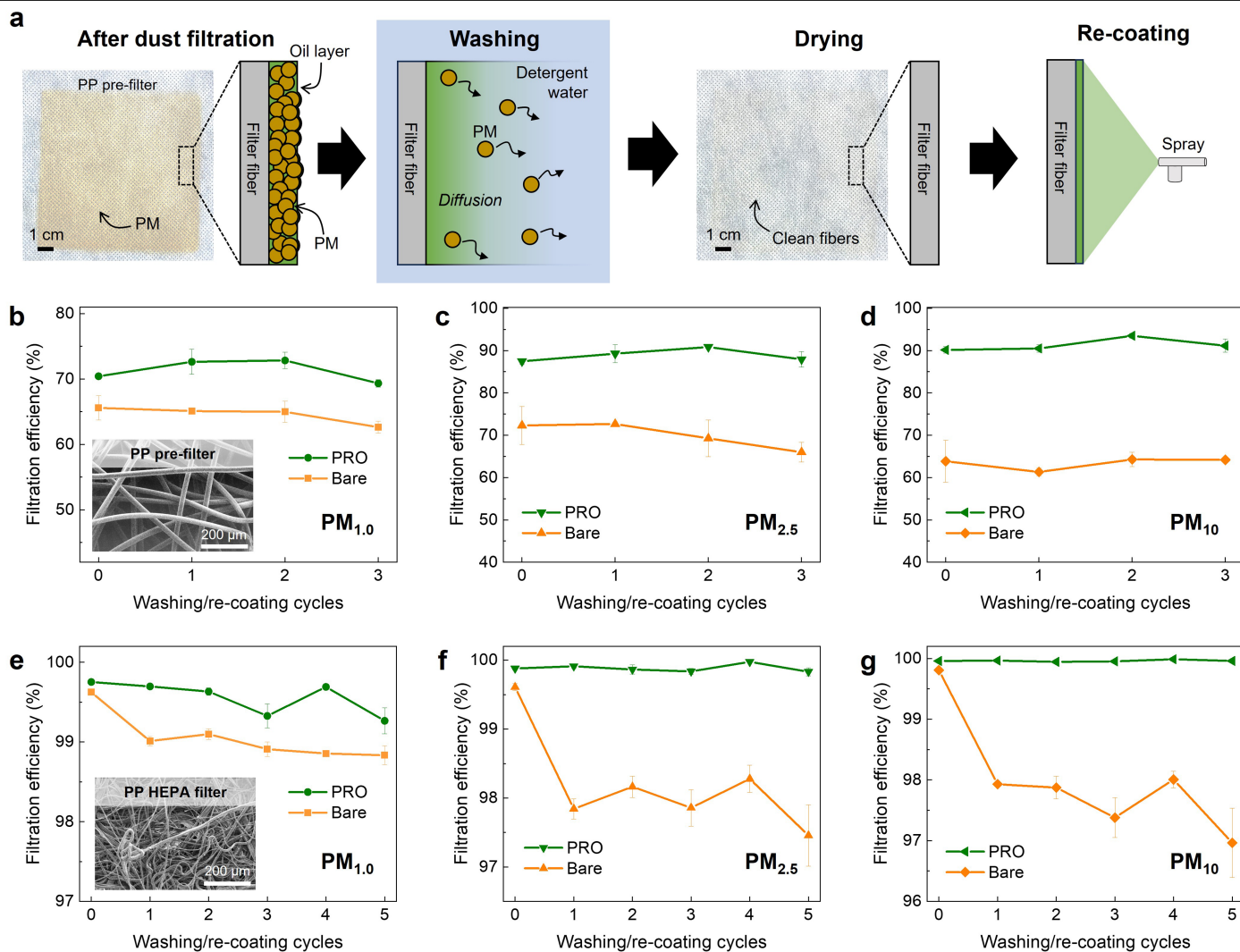
Extended Data Fig. 7 | Reusability test. a, Schematics of washing and PRO layer regeneration cycle. Photos indicate polypropylene (PP) pre-filter after filtration (left) and after washing with detergent water (middle). **b-d,** Filtration efficiencies of PP pre-filter with $PM_{1.0}$ (**b**), $PM_{2.5}$ (**c**), and PM_{10} (**d**) represented as a function of washing/re-coating cycles. Inset SEM image of $PM_{1.0}$ exhibits the structure of PP pre-filters. **e-g,** Filtration efficiencies of PP HEPA filter with $PM_{1.0}$ (**e**), $PM_{2.5}$ (**f**), and PM_{10} (**g**) represented as a function of washing cycles. Inset SEM image of $PM_{1.0}$ exhibits the structure of PP HEPA filter. Errors show s.d.; $n = 3$.
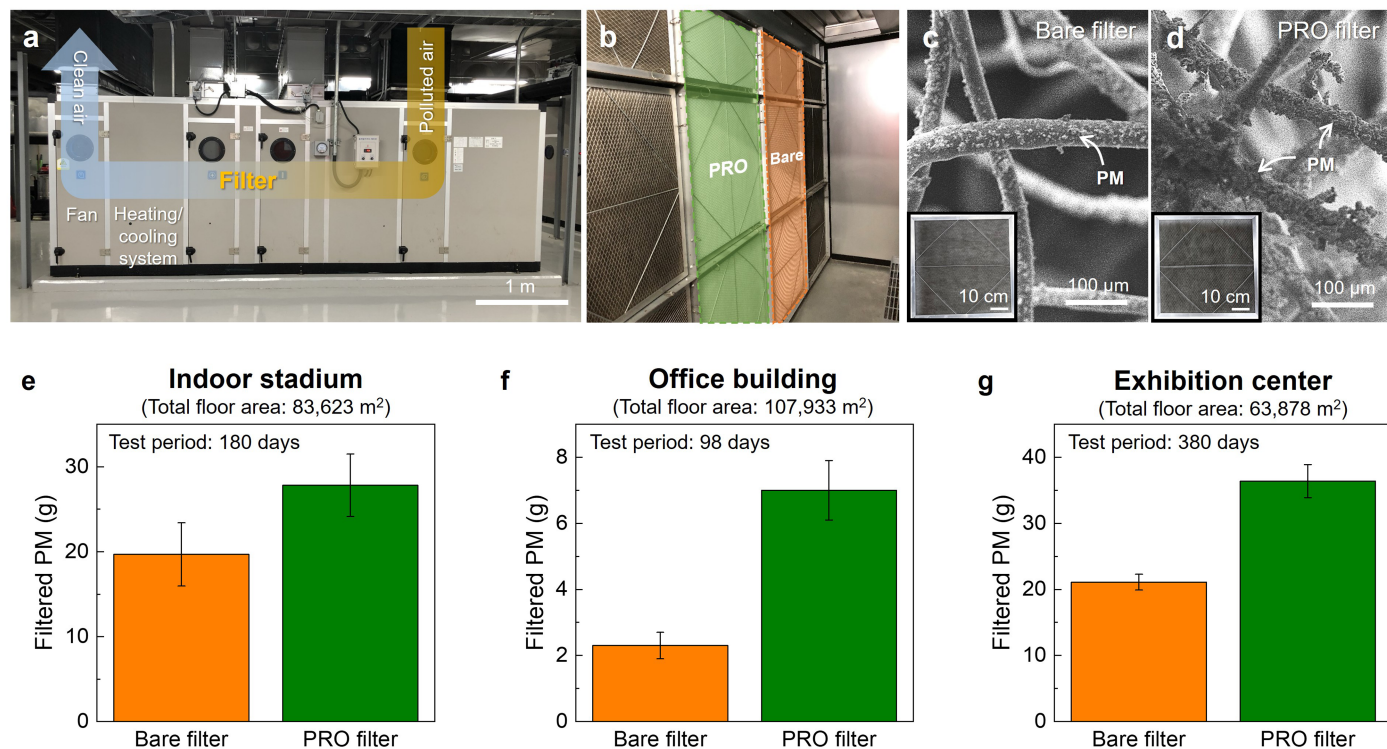
Extended Data Fig. 8 | Field filtration test. a, Photo of exterior of HVAC system. **b**, Photo of PRO (green) and bare (orange) filters simultaneously installed in the HVAC system. **c,d**, SEM images of bare (**c**) and PRO (**d**) filters after 4 months operation. Insets are real photos of the filters (dimension of 594 mm × 594 mm). **e-g**, Total weight of filtered PM of bare (orange bar) and PRO (green bar) filters operated in indoor stadium (**e**), office building (**f**), and exhibition center (**g**). Errors show s.d.; $n = 5$ for indoor stadium and 3 for office building and exhibition center.

Extended Data Table 1 | Filtering performances

Sample		Air permeability (cm³/s/cm²) at 125 Pa	Filtration efficiency (%)			Pressure drop (Pa)
			$PM_{1.0}$	$PM_{2.5}$	PM_{10}	
Polyester Non-woven	Bare	325.6 ± 4.0	22.1 ± 1.6	68.8 ± 1.7	81.4 ± 0.8	78.4 ± 0.8
	PRO	322.7 ± 6.0	29.7 ± 0.3	82.4 ± 0.4	94.6 ± 0.4	80.4 ± 0.9
Polypropylene Non-woven I	Bare	134.8 ± 1.9	66.8 ± 1.1	73.7 ± 2.9	68.9 ± 1.7	235.5 ± 4.0
	PRO	136.3 ± 3.0	70.4 ± 0.3	87.5 ± 0.5	90.2 ± 0.6	233.6 ± 3.0
Polyvinylidene fluoride Non-woven	Bare	130.0 ± 1.4	69.2 ± 0.2	80.5 ± 0.03	73.1 ± 0.3	224.7 ± 5.5
	PRO	128.6 ± 1.6	76.8 ± 1.5	93.0 ± 0.5	94.9 ± 0.5	233.9 ± 1.8
Melamine Foam	Bare	296.5 ± 2.5	48.1 ± 1.3	79.0 ± 0.6	82.5 ± 0.5	69.3 ± 0.5
	PRO	299.5 ± 4.3	50.2 ± 0.8	86.4 ± 0.6	93.3 ± 0.3	69.9 ± 1.2
Nickel Foam	Bare	> 500	12.3 ± 2.7	55.2 ± 2.5	62.1 ± 2.7	31.4 ± 0.5
	PRO	> 500	22.2 ± 0.7	68.3 ± 0.2	82.7 ± 0.7	32.0 ± 0.7
Cotton Woven I	Bare	75.3 ± 1.8	82.0 ± 0.1	84.7 ± 0.8	90.7 ± 0.6	607.9 ± 17.4
	PRO	74.1 ± 2.7	86.7 ± 0.1	94.2 ± 0.5	96.2 ± 0.2	562.2 ± 13.9
Cotton Woven II	Bare	155.4 ± 1.3	39.4 ± 3.2	50.9 ± 4.3	58.2 ± 2.1	226.1 ± 2.7
	PRO	153.7 ± 1.5	52.6 ± 0.6	73.1 ± 0.1	81.5 ± 0.3	228.7 ± 1.6
Hemp Woven	Bare	210.2 ± 1.4	16.5 ± 5.4	25.4 ± 7.0	26.8 ± 6.6	123.2 ± 3.2
	PRO	212.0 ± 1.4	25.8 ± 0.5	48.1 ± 0.7	59.8 ± 1.2	120.5 ± 0.5
Polypropylene Non-woven II	Bare	42.8 ± 0.9	97.4 ± 0.2	97.5 ± 0.2	98.6 ± 0.1	616.7 ± 12.6
	PRO	42.8 ± 0.4	97.7 ± 0.1	99.5 ± 0.1	99.7 ± 0.1	607.9 ± 12.7
Polypropylene Non-woven III	Bare	20.5 ± 0.3	99.2 ± 0.1	98.5 ± 0.1	99.5 ± 0.04	1071.5 ± 15.9
	PRO	21.3 ± 0.5	99.7 ± 0.1	99.7 ± 0.1	99.9 ± 0.02	1079.0 ± 24.0

Face velocity: 2 m/s (Flow late: 1.2 m³/min)

Filtering performances in detail, shown in Fig. 2a, including air permeability at 125 Pa, FE of $PM_{1.0}$ (0.3–1 µm in diameter), $PM_{2.5}$ (1–2.5 µm in diameter), and PM_{10} (2.5–10 µm in diameter) and ΔP. Testing area is 100 cm². Errors show s.d.; $n = 3$.